

Dose Prediction with U-net: A Feasibility Study for Predicting Dose Distributions from Contours using Deep Learning on Prostate IMRT Patients

Dan Nguyen, Troy Long, Xun Jia, Weiguo Lu, Xuejun Gu, Zohaib Iqbal, Steve Jiang

Center for Artificial Intelligence in Medicine and Department of Radiation Oncology, University of Texas Southwestern Medical Center, Dallas, TX, 75390, USA

E-mail: Dan.Nguyen@UTSouthwestern.edu

Abstract

With the advancement of treatment modalities in radiation therapy, outcomes have greatly improved, but at the cost of increased treatment plan complexity and planning time. The accurate prediction of dose distributions would alleviate this issue by guiding clinical plan optimization to save time and maintain high quality plans. We have developed a novel application of the fully convolutional deep network model, U-net, for predicting dose from patient contours. We show that with this model, we are able to accurately predict the dose of prostate cancer patients, where the average dice similarity coefficient is well over 0.9 when comparing the predicted vs. true isodose volumes between 0% and 100% of the prescription dose. The average differences in mean and max dose for all structures were within 2.3% of the prescription dose.

1 Introduction

Radiation therapy has been one of the leading treatment methods for cancer patients, and with the advent and advancements of innovative modalities, such as intensity modulated radiation therapy (IMRT)¹⁻⁷ and volume modulated arc therapy (VMAT)⁸⁻¹⁵, plan quality has drastically improved over the last few decades. However, such a development comes at the cost of treatment planning complexity. While this complexity has given rise to better plan quality, it is a double-edged sword that has also increased the planning time and obscured the tighter standards that these new treatment modalities are capable of meeting. The prediction of dose distributions and constraints has become an active field of research, with the goal of creating consistent plans that are informed by the ever-growing body of

treatment planning knowledge, as well guiding clinical plan optimization to save time and to maintain high quality treatment plans across planners of different experiences and skill levels.

Much of the work for dose prediction in radiotherapy has been revolving around a paradigm known as knowledge-based planning (KBP)¹⁶⁻²⁹, which has been focused on the prediction of a patient's dose distribution and dose volume histogram (DVH), using historical patient plans and information. While KBP has seen large successes and advancements that have improved the reliability of its predictions, these methods require the enumeration of parameters/features in order to feed into a model for dose and DVH prediction. Although much time and effort has been spent in selecting handcrafted features—such spatial information of organs at risk (OAR) and planning target volumes (PTV), distance-to-target histograms (DTH), overlapping volume histograms (OVH), structure shapes, number of delivery fields, etc.²¹⁻²⁹—it is still deliberated as to which features have the greatest impact and what other features would considerably improve the dose prediction. Artificial neural networks have been applied to learn more complex relationships between the handcrafted data²¹, but it is still limited by the inherent information present in that data.

In the last few years, deep learning has made a quantum leap in the advancement of many areas. One particular area was the progression of convolutional neural network (CNN)³⁰ architectures for imaging and vision purposes³¹⁻³³. In 2015, a radical idea called fully convolutional networks (FCN)³⁴ was proposed. It provided an architecture to make predictions at the pixel level instead of a coarse inference on images, and outperformed state-of-the-art techniques of its time at semantic segmentation. Shortly after, more complex models were built around the FCN concept in order to solve some of its shortcomings. One particular architecture that was proposed was a model called U-net³⁵, which focused on the semantic segmentation on biomedical images. Its success was largely attributed its ability to capture both local and global features in an image, due to three central ideas in the architecture design: 1) a large number of max pooling operations to allow for the convolution filters to find global, non-local features, 2) transposed convolution operations—also known as deconvolution³⁶ or up-convolution³⁵—to return the image to its original size, and 3) copying the maps from the first half of the U-net in order to preserve the lower-level, local features. These key ideas of the U-net make it ideal for the challenge of dose prediction in radiotherapy. While inserting some domain knowledge into the problem is essential due to a limited amount of data, we look towards deep learning to reduce our dependence on handcrafted features, and allow the deep network to learn its own features for prediction. We hypothesize that the U-net architecture will be able to accurately predict a dose distribution from simple patient contours, by learning to abstract its own high-level local and broad features.

2 Methods

2.1 U-net architecture for dose prediction

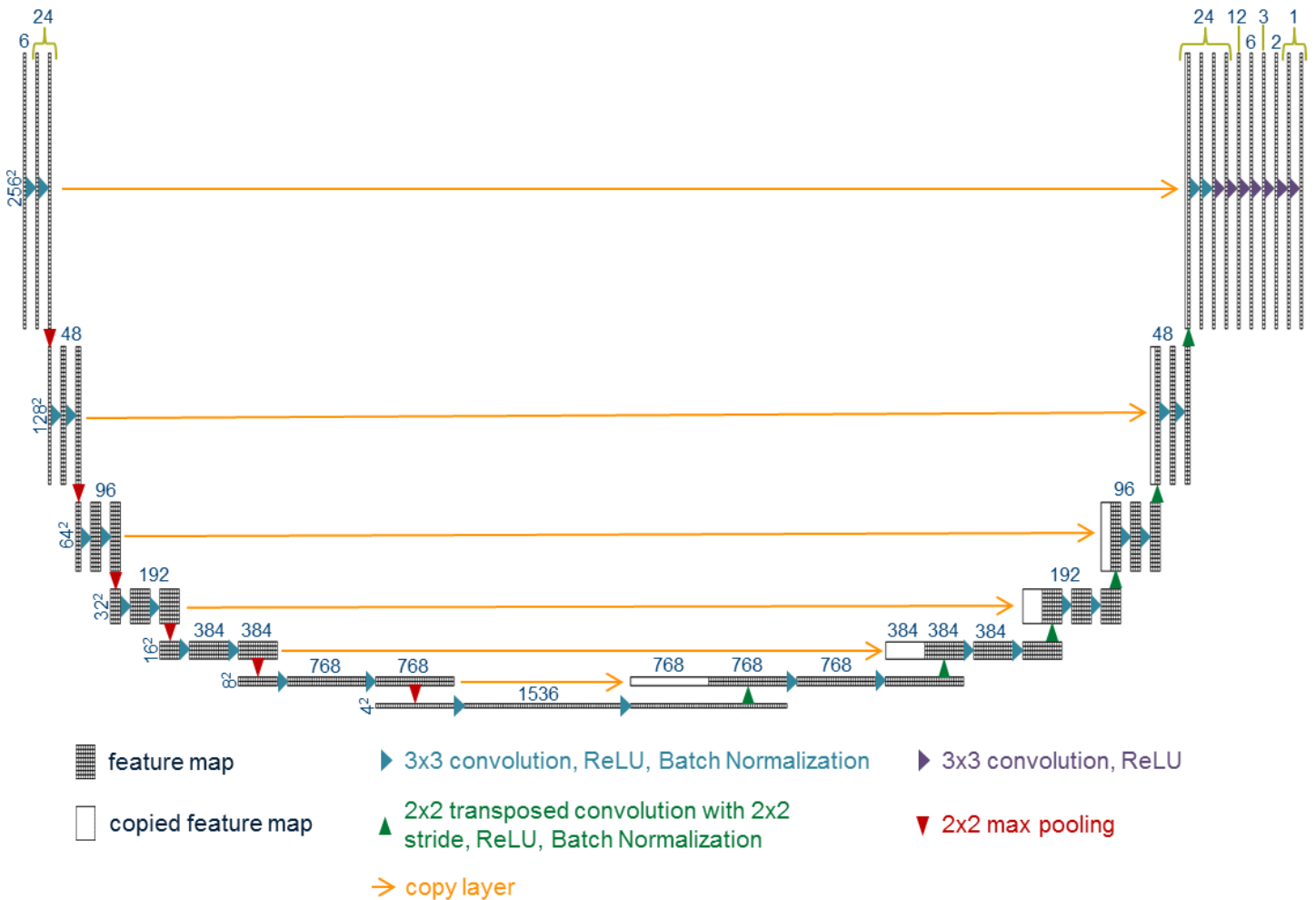


Figure 1: U-net architecture with additional CNN layers used for dose prediction. The numbers above the boxes represent the number of features for each map, while the numbers to the left of each hierarchy in the U-net represents the size of each 2D feature.

As shown in Figure 1, a seven-level hierarchy U-net was constructed, with a few extra modifications made on the original design achieve the goal of contour-to-dose mapping. The choice for 7 levels with 6 max pooling operations was made to reduce the feature size from 256 x 256 pixels down to 4 x 4 pixels, allowing for the 3 x 3 convolution operation to connect the center of the tumor to the edge of the body for all of the patient cases. Zero padding was added to the convolution process so that the feature size is maintained. Seven CNN layers, denoted with the purple arrows in Figure 1, were added after the U-net in order to smoothly reduce the number of filters to one. Batch normalization³⁷ (BN) was added after the convolution and rectified linear unit (ReLU) operations in the U-net, which

allows for a more equal updating of the weights throughout the U-net, leading to faster convergence. It should be noted that the original BN publication suggests performing the normalization process before the non-linearity operation, but we had found better performance using normalization after the ReLU operation—the validation’s mean squared error after 10 epochs was 0.3528 for using BN before ReLU and 0.0141 for using BN after ReLU. The input starts with 6 channels of 256 x 256 pixel images, with each channel representing a binary mask for 1 of the 6 contours used in this study.

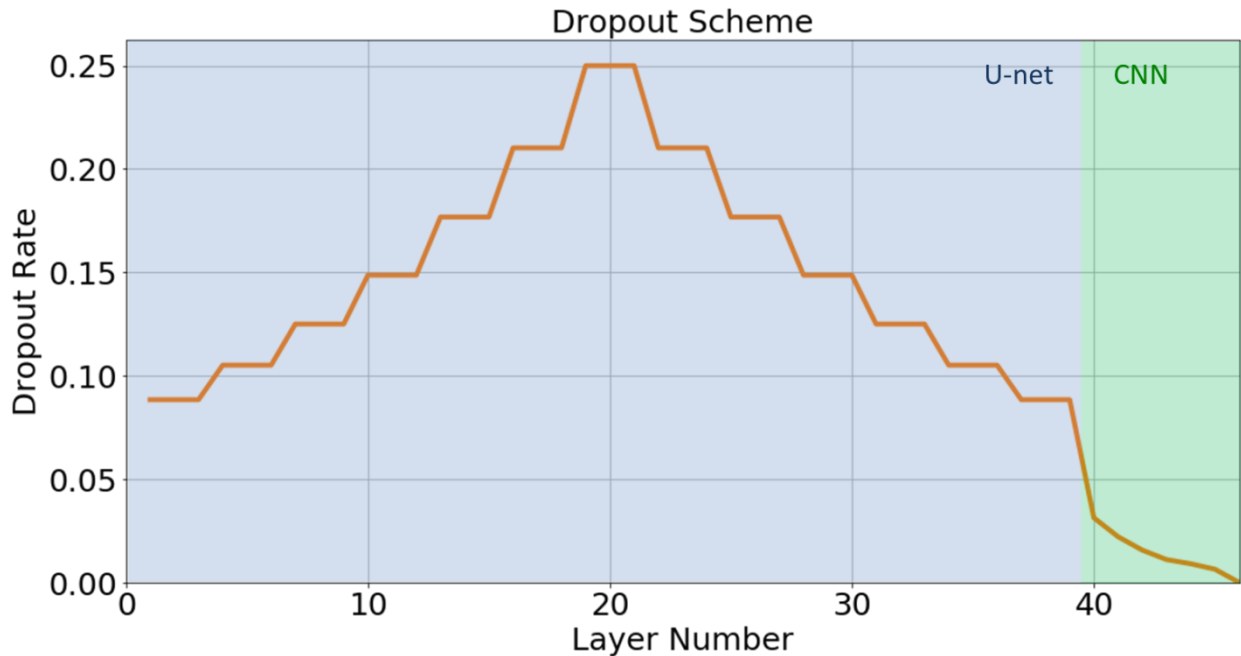


Figure 2: Dropout scheme implemented for the U-net and CNN layers

To prevent the model from overfitting, dropout³⁸ regularization was implemented according to the scheme shown in Figure 2, which is represented by the equation:

$dropout_{rate} = rate_{max} \times \left(\frac{current\ number\ of\ filters}{max\ number\ of\ filters} \right)^{1/n}$. For our particular setup, we chose $rate_{max} = 0.25$ and the $max\ number\ of\ filters = 1536$. We chose $n = 4$ for the U-net layers, and $n = 2$ for the added CNN layers. The choice for the dropout parameters was determined empirically, until the gap between the validation loss and training loss did not tend to increase during training.

The Adam algorithm³⁹ was chosen as the optimizer to minimize the loss function. In total, the network consisted of 46 layers. The deep network architecture was implemented in Keras⁴⁰ with Tensorflow⁴¹ as the backend.

2.2 Training and Evaluation

To test the feasibility of this model, treatment plans of 80 clinical coplanar IMRT prostate patients, each planned with 7 IMRT fields at 15 MV, were used. The 7 IMRT beam angles were similar across the 80 patients. Each patient had 6 contours: planning target volume (PTV), bladder, body, left femoral head, right femoral head, and rectum. The volume dimensions were reduced to 256 x 256 x 64 voxels, with resolutions of 2 x 2 x 2.5 mm³. For training, all patient doses were normalized such that the mean dose delivered to the PTV was equal to 1.

The U-net model was trained on single slices of the patient. As input, the 6 contours were each treated as their own channel in the image (analogous to how RGB images are treated as 3 separate channels in an image). The output is the U-net's prediction of the dose for that patient slice. The loss function was chosen to be the mean squared error between the predicted dose and the true dose delivered to the patient.

Since the central slices containing the PTV were far more important than the edge slices for dose prediction, we applied this domain knowledge into the problem by implementing a Gaussian sampling scheme—the center slice would more likely be chosen when the training function queried for another batch of random samples. The distance from the center slice to the edge slice was chosen to equal 3 standard deviations for the Gaussian sampling.

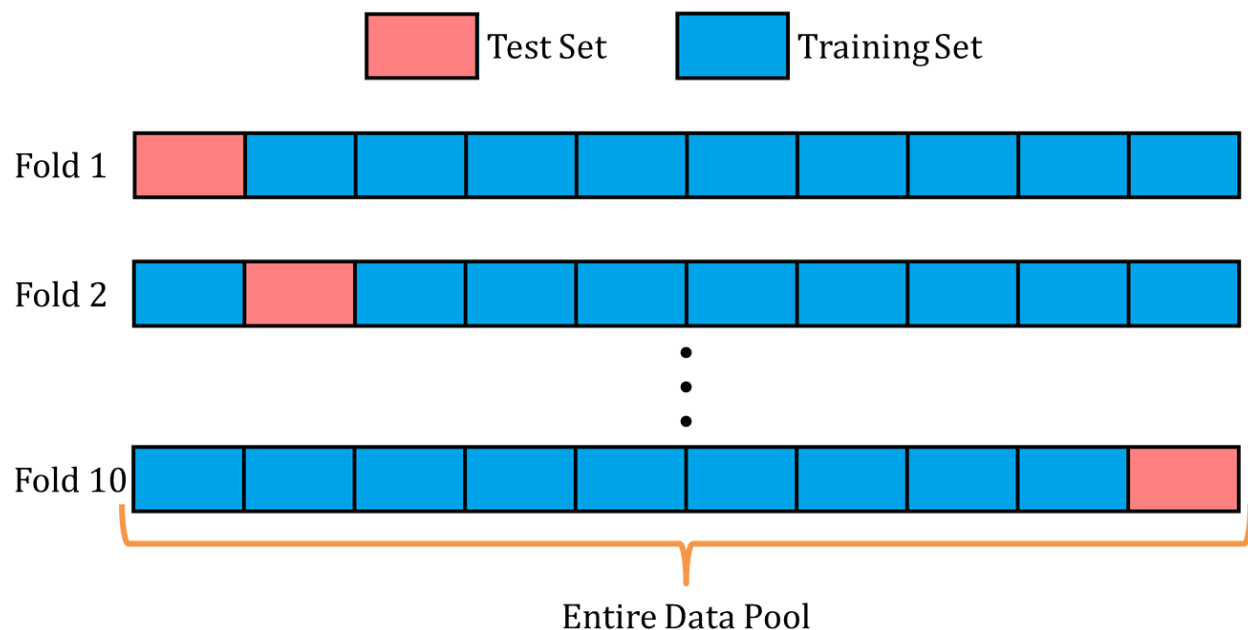


Figure 3: Schematic for 10-fold cross-validation.

To assess the overall performance of the model, a 10-fold cross-validation procedure was performed, as shown in Figure 3. Each of the 10 folds divides the 80 patients into 72

training patients and 8 test patients. Ten separate U-net models are initialized, trained, and validated on a unique training and test combination. Each fold produces a model that can predict the dose distribution on 8 patients it has never trained on. Combining the prediction results from all 10 models yields a total of 80 patients with valid dose predictions.

For the remainder of the manuscript, some common notation will be used. $D\#$ is the dose that $\#%$ of the volume of a structure of interest is at least receiving. V_{ROI} is the volume of the region of interest. For example, $D95$ is the dose that 95% of the volume of the structure of interest is at least receiving. V_{PTV} is the volume of the PTV and $V_{\# \% Iso}$ is the volume of the $\#%$ isodose region.

To compare across all 80 patients, all plans were normalized such that 95% of the PTV volume was receiving the prescription dose ($D95$). It should be noted that this is normalized differently than for training the model, which had normalized the plans by PTV mean dose. Normalizing by PTV mean dose creates a uniform dataset which is more likely to be stable for training, but plans normalized by $D95$ have more clinical relevance and value for assessment. All dose statistics will also be reported relative to the prescription dose (i.e. the prescription dose is set to 1). As evaluation criteria, dice similarity coefficients $\left(\frac{2(A \cap B)}{A+B}\right)$ of isodose volumes, structure mean and max doses, PTV $D98$, $D99$, D_{max} , PTV homogeneity $\left(\frac{D2-D98}{D50}\right)$, van't Reit conformation number⁴² $\left(\frac{(V_{PTV} \cap V_{100\%Iso})^2}{V_{PTV} \times V_{100\%Iso}}\right)$, and the dose spillage $R50$ $\left(\frac{V_{50\%Iso}}{V_{PTV}}\right)$, were evaluated.

Five NVIDIA Tesla K80 dual-GPU graphics cards (10 GPU chips total) were used in this study. One GPU was used for training each fold of the 10-fold cross-validation. Training batch size was chosen to be 24 slices.

3 Results

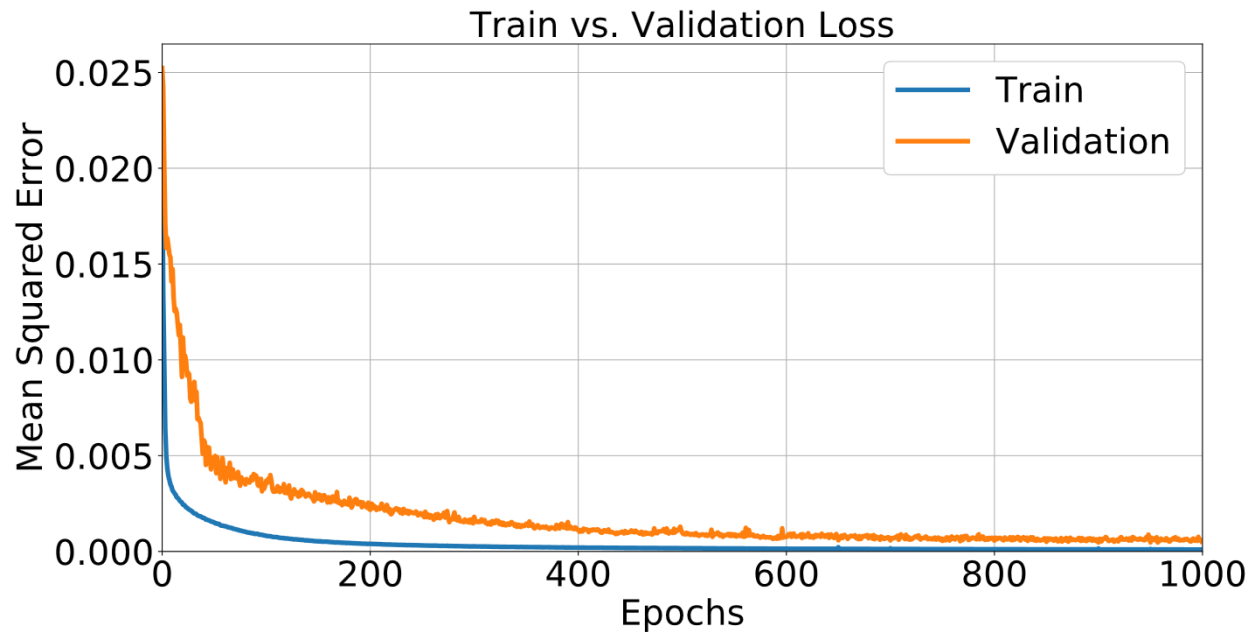


Figure 4: Plot of train vs. validation loss as a function of epochs from one of the folds.

In total, models from all folds trained for 1000 epochs each, which took approximately 6 days on the 10 GPUs. A plot of training and validation loss from one of the folds is shown in Figure 4 as an example. The final average loss \pm standard deviation between all the folds is $(1.02 \pm 0.05) \times 10^{-4}$ (training loss) and $(6.26 \pm 1.34) \times 10^{-4}$ (validation loss).

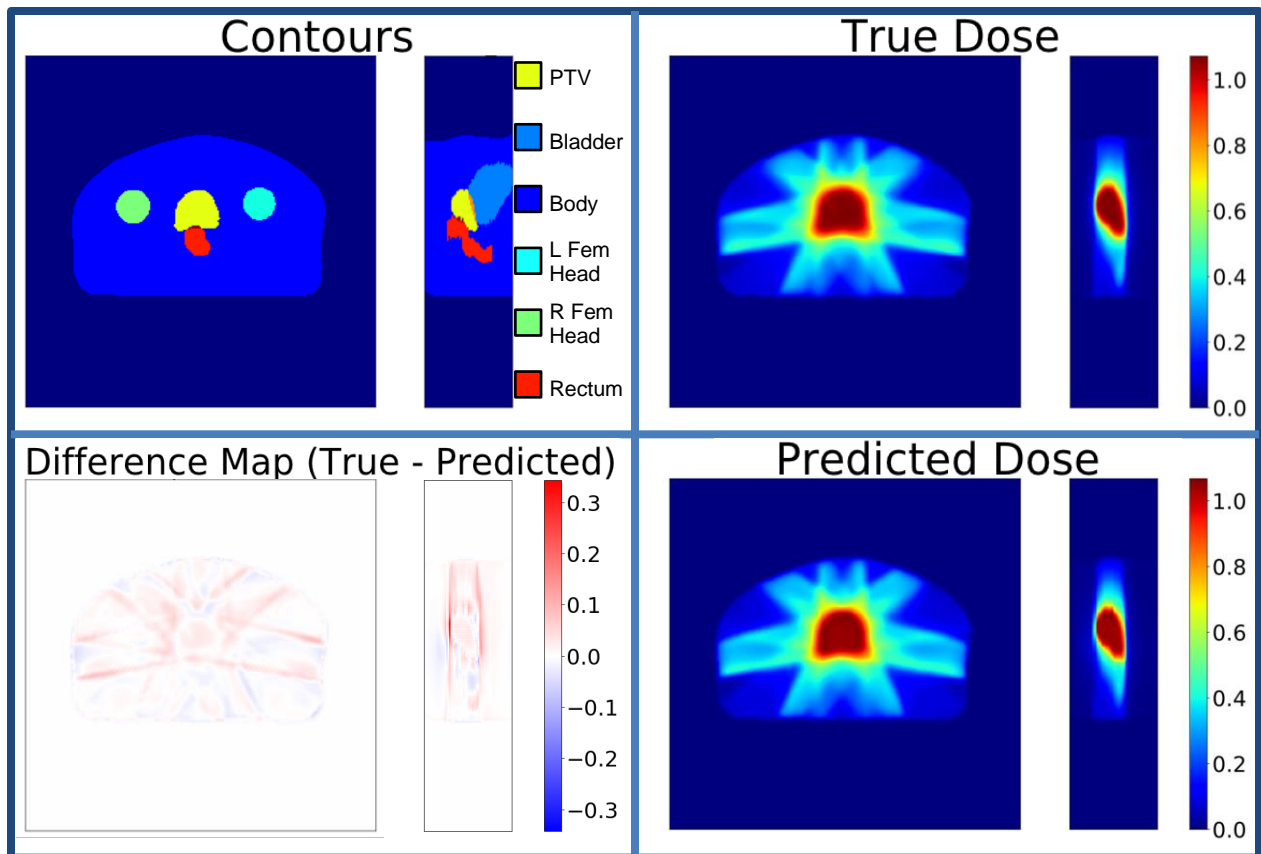


Figure 5: Contours of the planning target volume (PTV) and organs at risk (OAR), true dose wash, predicted dose wash, and difference map of one patient. Mean dose difference inside the body is 0.9% of the prescription dose.

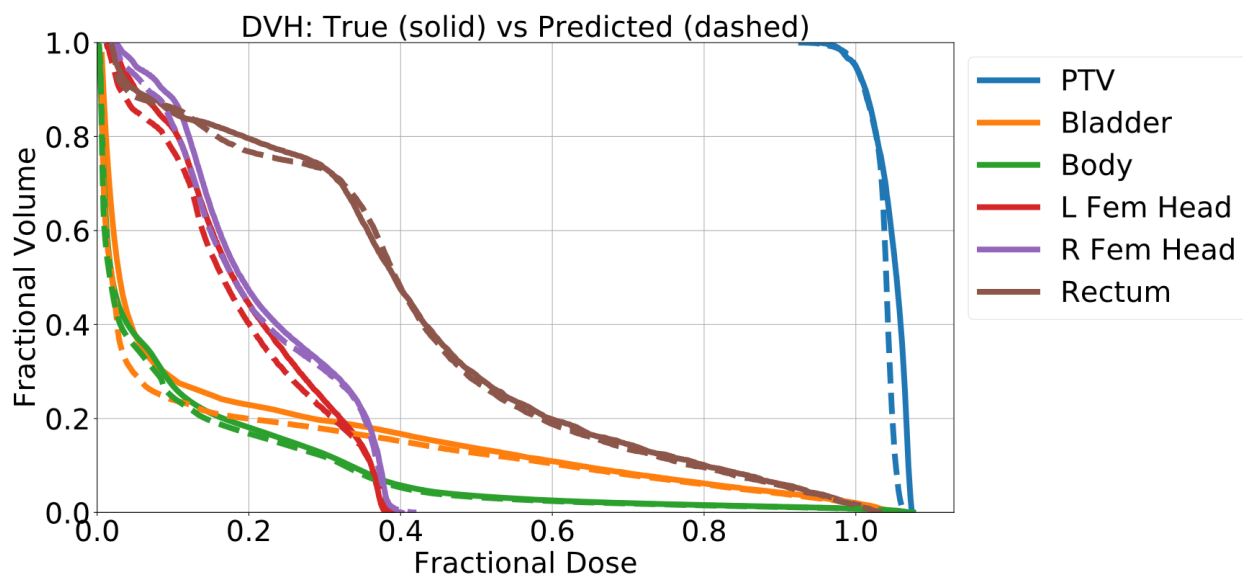


Figure 6: Example of typical dose volume histogram (DVH) comparing true dose and predicted dose for one patient.

As a typical prediction example from the U-net model, Figure 5 shows the input contours, true and predicted dose washes, and a difference map of the two doses for one patient. On average, the dose difference inside the body was less than 1% of the prescription dose. Figure 6 shows the DVH of the same patient as in Figure 5. Visually on the DVH, one can see that the U-net tends to predict a similar PTV dose coverage while slightly under-predicting the OAR doses.

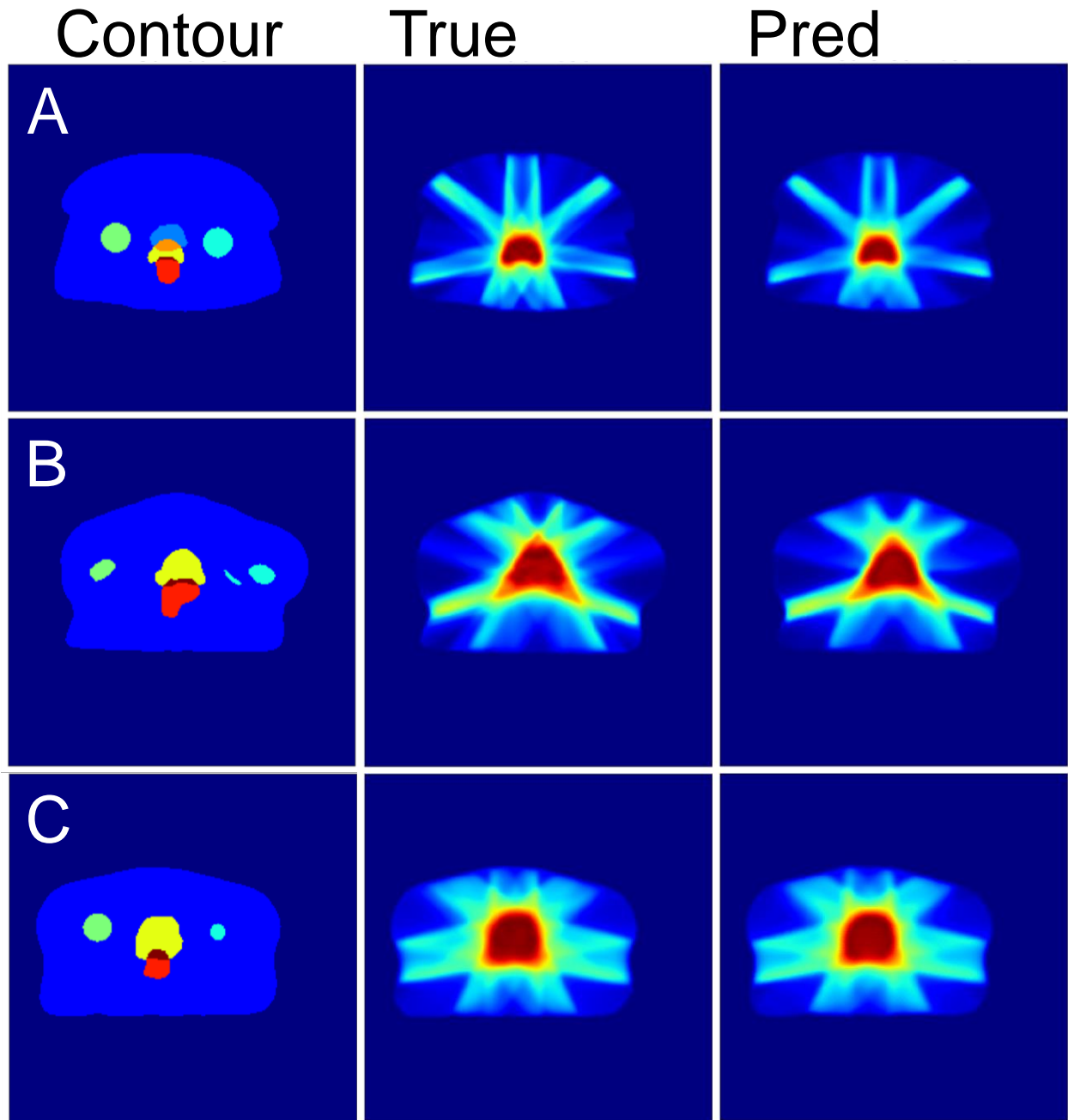


Figure 7: Example dose predictions from the U-net model on several patients with vastly different geometries.

Figure 7 shows some examples of dose prediction from the U-net on patients that have very diverse geometries. It can be visually seen that the U-net has learned to shape the dose based on the PTV and OARs sizes, locations, and shapes. The finer details of the dose distributions further away from the PTV have been correctly predicted by the deep network model.

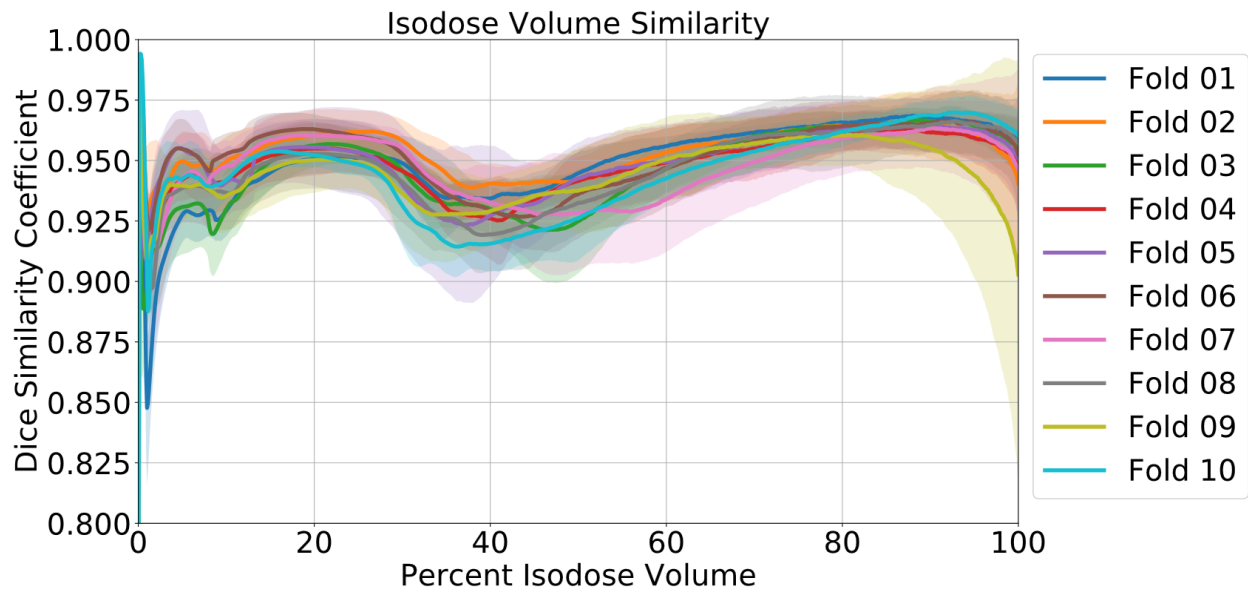


Figure 8: Dice similarity coefficients, $\frac{2(A \cap B)}{A+B}$, comparing isodose volumes between the true dose and predicted dose, ranging from the 0% isodose volume to the 100% isodose volume. The error in the graph represents 1 standard deviation.

Dice similarity coefficients range from 0 to 1, where 1 is considered a perfect match. The average dice similarity coefficients were well over 0.9 for most of the isodose volumes, as shown in Figure 8. All cross-validation folds shared similar trends in the isodose volume similarity, expressing slight decreases in the dice coefficient near the 1% isodose volume, the 40% isodose volume, and the 100% isodose volume. It is not entirely clear as to why the U-net model has more difficulty with predicting the dose in these areas. Further investigation will be conducted on this matter.

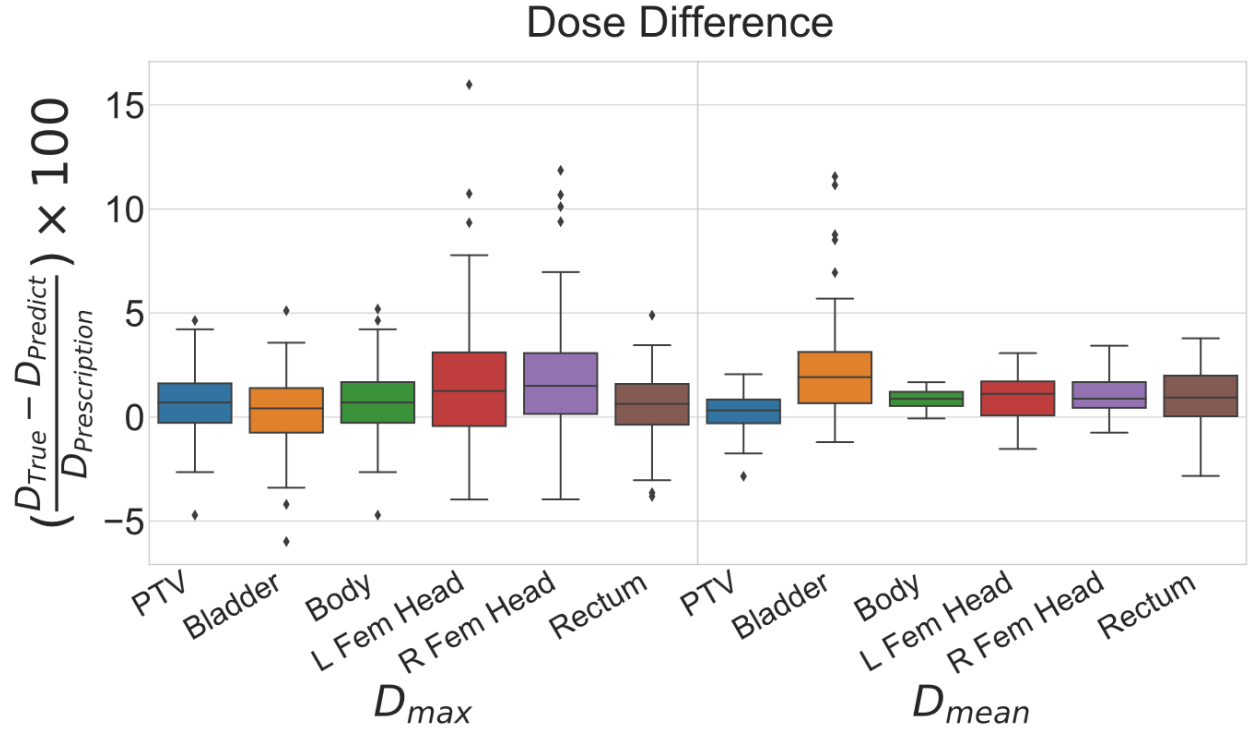


Figure 9: Box plots showing the dose difference statistics for all 80 patients.

	Average Dose Difference $\left(\frac{D_{True} - D_{Prediction}}{D_{Prescription}} \right) \times 100$	
	mean value \pm standard deviation	
	D_{max}	D_{mean}
PTV	0.70 ± 1.66	0.22 ± 0.94
Bladder	0.38 ± 1.77	2.28 ± 2.36
Body	0.75 ± 1.73	0.86 ± 0.43
L Fem Head	1.71 ± 3.11	0.92 ± 1.01
R Fem Head	1.81 ± 2.92	1.12 ± 0.95
Rectum	0.59 ± 1.58	0.97 ± 1.42

Table 1: Average differences in mean and max dose with standard deviations.

A box plot of max and mean dose differences (True - Prediction) for the PTV and OARs are shown in Figure 9. The median values on the box plot are slightly positive, showing that the U-net tends to under-predict the doses. These under-predictions are very minor, where the largest average difference in the max dose was for the right femoral head at 1.81% of the prescription dose. The average largest difference in mean dose was found to be the bladder at 2.28% of the prescription dose. A full list of average differences can be found in Table 1.

	True Values	Predicted Values	True - Predicted
	mean value \pm standard deviation		
PTV D98	0.98 ± 0.01	0.98 ± 0.01	-0.001 ± 0.010
PTV D99	0.97 ± 0.01	0.97 ± 0.04	0.002 ± 0.035
PTV D_{max}	1.08 ± 0.02	1.08 ± 0.02	0.007 ± 0.017
PTV Homogeneity	0.09 ± 0.02	0.08 ± 0.03	0.008 ± 0.018
van't Riet Conformation Number	0.88 ± 0.08	0.92 ± 0.04	-0.037 ± 0.048
R50	4.45 ± 1.23	4.10 ± 1.14	0.350 ± 0.231

Table 2: True and predicted values for PTV statistics, homogeneity, van't Riet conformation number, and the high dose spillage, R50.

PTV D_{98} , D_{99} , D_{max} , and homogeneity were very similar between the true and predicted values, as shown in Table 2. Some larger differences are found for van't Riet Conformation Number and the high dose spillage, R50. On average, the U-net model tends to predict a more conformal dose with less dose spillage outside the PTV.

4 Discussion

A clear trend for the U-net model is that it would tend to predict a more conformal dose with less dose spillage outside the PTV, while also slightly under-predicting doses to organs at risk. Most likely this is caused by the U-net making some averages in the higher order heterogeneities in the dose between different patient cases. This error is very slight, being under 2.3% for prediction of OAR mean and max doses. In practice this OAR under-prediction can be beneficial if used as a planning guidance tool where planners try to meet the criteria outlined by the model.

The 80 clinical prostate patients acquired in this study used a similar set of 7 beam angles and criteria for treatment, giving rise to some uniformity to the data that made it ideal as a test bed to investigate the feasibility for dose prediction using a deep learning model. However, the current model architecture and data leave the U-net with several limitations. First, the model has currently learned to only predict the dose coming from approximately the same orientations, and may not be able to account for more intricate beam geometries. Secondly, the current model is unable to account for any physician preferences for predicting the dose, limiting the level of treatment personalization for the patient. For example, the model is unable to create a rectum-sparing plan or a bladder-sparing plan, at the will of the physician, for the same patient geometry. Furthermore, while training slice-by-slice had proven successful for coplanar cases, this method may not perform satisfactorily when performing dose prediction for non-coplanar plans. The deep network

may have to understand the patient geometry in 3D if it were to start accounting for non-coplanar beam dose.

We plan to extend this study by building a deep learning model for learning dose predictions that is capable of handling a more diverse selection of non-coplanar beam orientations. We will investigate the extension of U-nets into the volumetric domain using V-nets⁴³, in order to tackle dose prediction for non-coplanar radiotherapy plans, and add in dose constraint parameters into the model input to allow the prediction of dose based on the physician's prescription, not only patient's geometry.

5 Conclusion

We have developed a novel application of the fully convolutional deep network model, U-net, for dose prediction. The model is able to take a prostate patient's contours and then predict a dose distribution by abstracting the contours into local and global features. Using our implementation of U-net we are able to accurately predict the dose of a patient, with average mean and max dose differences of all structures within 2.3% of the prescription dose. Isodose similarity evaluation reveals that the predicted dose isodose volumes match the true isodose volumes with the average dice coefficient well over 0.9. We plan to continue improving the model, by adding in dose prediction for non-coplanar beam arrangements and accounting for physician preference. The immediate application of the dose prediction model is to guide clinical plan optimization to reduce treatment planning time and to maintain high quality plans. The long-term objective is to incorporate the learning dose prediction model into an artificially intelligent radiation therapy treatment planner.

6 Acknowledgements

This study was supported by the Cancer Prevention & Research Institute of Texas (CPRIT) IIRA RP150485.

7 References

1. Brahme A. Optimization of stationary and moving beam radiation therapy techniques. *Radiotherapy and Oncology*. 1988;12(2):129-140.
2. Bortfeld T, Bürkelbach J, Boesecke R, Schlegel W. Methods of image reconstruction from projections applied to conformal radiotherapy. *Physics in Medicine and Biology*. 1990;35(10):1423.
3. Bortfeld TR, Kahler DL, Waldron TJ, Boyer AL. X-ray field compensation with multileaf collimators. *International Journal of Radiation Oncology* Biology* Physics*. 1994;28(3):723-730.
4. Webb S. Optimisation of conformal radiotherapy dose distribution by simulated annealing. *Physics in Medicine and Biology*. 1989;34(10):1349.
5. Convery D, Rosenbloom M. The generation of intensity-modulated fields for conformal radiotherapy by dynamic collimation. *Physics in Medicine and Biology*. 1992;37(6):1359.
6. Xia P, Verhey LJ. Multileaf collimator leaf sequencing algorithm for intensity modulated beams with multiple static segments. *Medical Physics*. 1998;25(8):1424-1434.
7. Keller-Reichenbecher M-A, Bortfeld T, Levegrün S, Stein J, Preiser K, Schlegel W. Intensity modulation with the "step and shoot" technique using a commercial MLC: A planning study. *International Journal of Radiation Oncology* Biology* Physics*. 1999;45(5):1315-1324.
8. Yu CX. Intensity-modulated arc therapy with dynamic multileaf collimation: an alternative to tomotherapy. *Physics in Medicine and Biology*. 1995;40(9):1435.
9. Otto K. Volumetric modulated arc therapy: IMRT in a single gantry arc. *Medical physics*. 2008;35(1):310-317.
10. Palma D, Vollans E, James K, et al. Volumetric Modulated Arc Therapy for Delivery of Prostate Radiotherapy: Comparison With Intensity-Modulated Radiotherapy and Three-Dimensional Conformal Radiotherapy. *International Journal of Radiation Oncology* Biology* Physics*. 2008;72(4):996-1001.
11. Shaffer R, Morris WJ, Moiseenko V, et al. Volumetric Modulated Arc Therapy and Conventional Intensity-modulated Radiotherapy for Simultaneous Maximal Intraprostatic Boost: a Planning Comparison Study. *Clinical Oncology*. 2009;21(5):401-407.
12. Shaffer R, Nichol AM, Vollans E, et al. A Comparison of Volumetric Modulated Arc Therapy and Conventional Intensity-Modulated Radiotherapy for Frontal and Temporal High-Grade Gliomas. *International Journal of Radiation Oncology* Biology* Physics*. 2010;76(4):1177-1184.
13. Xing SMCaXWaCTaMWaL. Aperture modulated arc therapy. *Physics in Medicine & Biology*. 2003;48(10):1333.
14. Earl M, Shepard D, Naqvi S, Li X, Yu C. Inverse planning for intensity-modulated arc therapy using direct aperture optimization. *Physics in medicine and biology*. 2003;48(8):1075.
15. Daliang Cao and Muhammad KNAaJYaFCaDMS. A generalized inverse planning tool for volumetric-modulated arc therapy. *Physics in Medicine & Biology*. 2009;54(21):6725.

16. Zhu X, Ge Y, Li T, Thongphiew D, Yin FF, Wu QJ. A planning quality evaluation tool for prostate adaptive IMRT based on machine learning. *Medical physics*. 2011;38(2):719-726.
17. Appenzoller LM, Michalski JM, Thorstad WL, Mutic S, Moore KL. Predicting dose-volume histograms for organs-at-risk in IMRT planning. *Medical physics*. 2012;39(12):7446-7461.
18. Wu B, Pang D, Lei S, et al. Improved robotic stereotactic body radiation therapy plan quality and planning efficacy for organ-confined prostate cancer utilizing overlap-volume histogram-driven planning methodology. *Radiotherapy and Oncology*. 2014;112(2):221-226.
19. Shiraishi S, Tan J, Olsen LA, Moore KL. Knowledge-based prediction of plan quality metrics in intracranial stereotactic radiosurgery. *Medical physics*. 2015;42(2):908-917.
20. Moore KL, Brame RS, Low DA, Mutic S. Experience-Based Quality Control of Clinical Intensity-Modulated Radiotherapy Planning. *International Journal of Radiation Oncology*Biography*Physics*. 2011;81(2):545-551.
21. Shiraishi S, Moore KL. Knowledge-based prediction of three-dimensional dose distributions for external beam radiotherapy. *Medical physics*. 2016;43(1):378-387.
22. Wu B, Ricchetti F, Sanguineti G, et al. Patient geometry-driven information retrieval for IMRT treatment plan quality control. *Medical Physics*. 2009;36(12):5497-5505.
23. Wu B, Ricchetti F, Sanguineti G, et al. Data-Driven Approach to Generating Achievable Dose-Volume Histogram Objectives in Intensity-Modulated Radiotherapy Planning. *International Journal of Radiation Oncology*Biography*Physics*. 2011;79(4):1241-1247.
24. Wu B, Pang D, Simari P, Taylor R, Sanguineti G, McNutt T. Using overlap volume histogram and IMRT plan data to guide and automate VMAT planning: A head-and-neck case study. *Medical Physics*. 2013;40(2):021714-n/a.
25. Tran A, Woods K, Nguyen D, et al. Predicting liver SBRT eligibility and plan quality for VMAT and 4 π plans. *Radiation Oncology*. 2017;12(1):70.
26. Yuan L, Ge Y, Lee WR, Yin FF, Kirkpatrick JP, Wu QJ. Quantitative analysis of the factors which affect the interpatient organ-at-risk dose sparing variation in IMRT plans. *Medical Physics*. 2012;39(11):6868-6878.
27. Lian J, Yuan L, Ge Y, et al. Modeling the dosimetry of organ-at-risk in head and neck IMRT planning: An intertechnique and interinstitutional study. *Medical Physics*. 2013;40(12):121704-n/a.
28. Folkerts MM, Gu X, Lu W, Radke RJ, Jiang SB. SU-G-TeP1-09: Modality-Specific Dose Gradient Modeling for Prostate IMRT Using Spherical Distance Maps of PTV and Isodose Contours. *Medical Physics*. 2016;43(6Part26):3653-3654.
29. Folkerts MM, Long T, Radke RJ, et al. Knowledge-Based Automatic Treatment Planning for Prostate IMRT Using 3-Dimensional Dose Prediction and Threshold-Based Optimization. Presented at: American Association of Physicists in Medicine 2017; Denver, CO.
30. LeCun Y, Boser B, Denker JS, et al. Backpropagation applied to handwritten zip code recognition. *Neural computation*. 1989;1(4):541-551.

31. Krizhevsky A, Sutskever I, Hinton GE. Imagenet classification with deep convolutional neural networks. Paper presented at: Advances in neural information processing systems2012.
32. Girshick R, Donahue J, Darrell T, Malik J. Rich feature hierarchies for accurate object detection and semantic segmentation. Paper presented at: Proceedings of the IEEE conference on computer vision and pattern recognition2014.
33. Simonyan K, Zisserman A. Very deep convolutional networks for large-scale image recognition. *arXiv preprint arXiv:14091556*. 2014.
34. Long J, Shelhamer E, Darrell T. Fully convolutional networks for semantic segmentation. Paper presented at: Proceedings of the IEEE Conference on Computer Vision and Pattern Recognition2015.
35. Ronneberger O, Fischer P, Brox T. U-net: Convolutional networks for biomedical image segmentation. Paper presented at: International Conference on Medical Image Computing and Computer-Assisted Intervention2015.
36. Noh H, Hong S, Han B. Learning deconvolution network for semantic segmentation. Paper presented at: Proceedings of the IEEE International Conference on Computer Vision2015.
37. Ioffe S, Szegedy C. Batch normalization: Accelerating deep network training by reducing internal covariate shift. Paper presented at: International Conference on Machine Learning2015.
38. Srivastava N, Hinton GE, Krizhevsky A, Sutskever I, Salakhutdinov R. Dropout: a simple way to prevent neural networks from overfitting. *Journal of machine learning research*. 2014;15(1):1929-1958.
39. Kingma D, Ba J. Adam: A method for stochastic optimization. *arXiv preprint arXiv:14126980*. 2014.
40. Chollet F. Keras. In. <https://github.com/fchollet/keras>: Github; 2015.
41. Abadi M, Agarwal A, Barham P, et al. Tensorflow: Large-scale machine learning on heterogeneous distributed systems. *arXiv preprint arXiv:160304467*. 2016.
42. Van't Riet A, Mak AC, Moerland MA, Elders LH, van der Zee W. A conformation number to quantify the degree of conformality in brachytherapy and external beam irradiation: application to the prostate. *International Journal of Radiation Oncology* Biology* Physics*. 1997;37(3):731-736.
43. Milletari F, Navab N, Ahmadi S-A. V-net: Fully convolutional neural networks for volumetric medical image segmentation. Paper presented at: 3D Vision (3DV), 2016 Fourth International Conference on2016.